Thin Solid Films 662 (2018) 60–69

Contents lists available at ScienceDirect

Thin Solid Films

journal homepage: www.elsevier.com/locate/tsf

Electrical and chemical characterizations of hafnium (IV) oxide films for biological lab-on-a-chip devices

J.L. Collins[a], H. Moncada Hernandez[a], S. Habibi[a], C.E. Kendrick[b], Z. Wang[a], N. Bihari[b], P.L. Bergstrom[b], A.R. Minerick[a,*]

[a] Department of Chemical Engineering, Michigan Technological University, 1400 Townsend Drive, Houghton, MI 49931, USA
[b] Department of Electrical and Computer Engineering, Michigan Technological University, 1400 Townsend Drive, Houghton, MI 49931, USA

ARTICLE INFO

Keywords:
Hafnium oxide
Biocompatibility
Dielectric
Thin film characterization
Passivation
Lab-on-a-chip
Microdevices
Optically transparent

ABSTRACT

Many biological lab-on-a-chip applications require electrical and optical manipulation as well as detection of cells and biomolecules. This provides an intriguing challenge to design robust microdevices that resist adverse electrochemical side reactions yet achieve optical transparency. Physical isolation of biological samples from microelectrodes can prevent contamination, electrode fouling, and electrochemical byproducts; thus this manuscript explores hafnium oxide (HfO_2) films - originating from traditional transistor applications – for suitability in electrokinetic microfluidic devices for biological applications. HfO_2 films with deposition times of 6.5, 13, and 20 min were sputter deposited onto silicon and glass substrates. The structural, optical, and electrical properties of the HfO_2 films were investigated using atomic force microscopy (AFM), X-ray diffraction, energy dispersive X-ray spectroscopy, Fourier transform infrared spectroscopy, ellipsometry, and capacitance voltage. Electric potential simulations of the HfO_2 films and a biocompatibility study provided additional insights. Film grain size after corrosive Piranha treatment was observed via AFM. The crystalline structure investigated via X-ray diffraction revealed all films exhibited the (111) characteristic peak with thicker films exhibiting multiple peaks indicative of anisotropic structures. Energy dispersive X-ray spectroscopy via field emission scanning electron microscopy and Fourier transform infrared spectroscopy both corroborated the atomic ratio of the films as HfO_2. Ellipsometry data from Si yielded thicknesses of 58, 127, and 239 nm and confirmed refractive index and extinction coefficients within the normal range for HfO_2; glass data yielded unreliable thickness verifications due to film and substrate transparency. Capacitance-voltage results produced an average dielectric constant of 20.32, and the simulations showed that HfO_2 dielectric characteristics were sufficient to electrically passivate planar microelectrodes. HfO_2 biocompatibility was determined with human red blood cells by quantifying the hemolytic potential of the HfO_2 films. Overall results support hafnium oxide as a viable passivation material for biological lab-on-a-chip applications.

1. Introduction

1.1. Electrode isolation in lab-on-a-chip technology

Lab-on-a-chip (LOC) technologies and applications are continually expanding with an emphasis on electrical manipulations for chemical/biological detection. LOCs are prevalent in point-of-care clinical diagnostics due to the small sample and reagent volumes, cost effectiveness, rapid analyses, high sensitivity/selectivity, and potential for disposable devices [1]. For electric field utilization, electrode miniaturization improves sensitivity and device footprint [2]. However, electrode behaviors and subsequent solution characteristics are closely intertwined [3, 4]. Aqueous experimental samples in contact with electrodes can lead to electrode fouling [5, 6]. For example, platinum microelectrodes showed both morphological and chemical changes when exposed to biological buffer solutions in both AC and DC electric fields. These changes included oxidation and dissolution of platinum along with potassium deposition and chloride formation originating from buffer solutions [7]. Electrodes in contact with aqueous experimental samples can generate pH changes, target analyte interferences, and other byproducts. While electrode byproducts are sometimes harnessed for beneficial LOC functions: electrochemical impedance can detect foodborne pathogens [8], enzyme-catalyzed reactions can detect multiple metabolic biomarkers [9], and amperometric flow injection analysis

* Corresponding author.
E-mail address: minerick@mtu.edu (A.R. Minerick).

https://doi.org/10.1016/j.tsf.2018.07.024
Received 8 January 2018; Received in revised form 3 July 2018; Accepted 17 July 2018
Available online 18 July 2018

Table 1
Hafnium oxide in biological applications.

Ref.	Deposition method	HfO_2 (nm)	Substrate	Application	Characterization methods
[20]	ALD	~2.8, 45	Si (100) Prime grade 1–Ωcm	Charged based biosensors	SE, AFM, CV, XPS
[36]	ALD	13	Si-NW on Si-O-I p-type doped	Small nucleic acid oligomer detection	SE, AFM, SEM, CV, FLIC
[37, 38]	ALD	2–7	$Si/SiO_2/SiN_x$	DNA transport through nanopores and Protein analysis	AFM, CV, EDS, TEM
[39]	ALD	10	Si-NW on Si-O-I	Cardiac troponin 1 detection (biosensor)	TEM
[40]	ALD	16	Graphene/TiO_2 and Si, p-type, highly doped	Nanopores for biosensing	FFT, Contact angle, IV, Leakage current, TEM

can sense cholesterol [10], this is not uniformly desired.

Creative strategies to achieve electrode and target sample isolation include remote positioning of electrodes, membrane isolation, and passivation layers. In dielectrophoretic applications, insulating structures within channels replace embedded microelectrodes and effectively shape non-uniform electric fields (insulator dielectrophoresis) [6, 11, 12]. Membranes isolate electrode wells from LOC channels preventing unwanted electrode/solution effects, such as electrolysis bubbles [13]. A key approach is to apply dielectric thin film coatings over planar electrode surfaces as passivation layers to reduce ion production, Faradaic reactions, and electrode surface fouling [3, 7, 14, 15]. In electrowetting on dielectric (EWOD) devices, a dielectric layer is deposited on top of the electrodes to energize droplet motion across surfaces without causing solution interferences [16]. Some LOC applications desire complete electrical passivation from the fluidics [17]. In cell culturing, sensing windows monitored spreading kinetics via impedance while the remaining electrode region was passivated to isolate cells and reduce the risk of contamination from and reaction with electrode surfaces [17]. Thus, passivation layers over electrodes are a viable and growing method to selectively isolate electrodes from samples and preventing unwanted electrochemical byproducts.

1.2. Choosing a passivation layer

In electronics, high dielectric constant passivation in capacitors, resistors, and transistors improves performance during miniaturization. This knowledge can be translated into LOC applications bridging electronics and fluidics. The most common high dielectric constant shielding material is silicon dioxide (SiO_2). At thicknesses < 1.5 nm, SiO_2 has physical and electrical limitations that manifest in a leakage current [18, 19]. While leakage current is desired in some LOC applications, aqueous electrolyte solutions required for many biological applications can cause alkali ion contamination in the SiO_2 leading to undesirable device instability [20]. Common SiO_2 replacements include HfO_2, Si_3N_4, La_2O_3, Al_2O_3, ZrO_2, TiO_2, HfSiO, CeO_2, and $LaAlO_3$ [19–21]. Dielectric constants for these materials range from 3.9 for SiO_2 to 80 for TiO_2; the material explored here, HfO_2, is 20–25 [22].

In LOC devices, passivation materials must withstand mechanical/chemical stresses and not interfere with electric field characteristics or detection schemas at fluidic interfaces [23]. Passivation layer characteristics frequently assessed are dielectric strength and biocompatibility, along with mechanical, chemical, thermal, and charge stability [24], and are tailored to the application. LOC passivation materials have included Teflon, Parylene C, polydimethylsiloxane, polyimide, silicon dioxide, silicon nitride, SU-8, dry-film, and others [16, 23–26].

Biological LOCs require films with optical transparency and biocompatibility. Optical transparency within LOCs enables optical detection techniques such as absorbance, reflectance, fluorescence, and chemiluminescence, among others [27]. Common biocompatible passivation materials include cover glass, photoresist, epoxy, polyimide, SiO_2, and Si_3N_4 [17]. However, these materials display undesirable refractive properties, limited optical transparency, and/or non-ideal electrical passivation characteristics. HfO_2 stability in aqueous solutions and biomolecule functionalization was demonstrated [20]. Thus, this work investigated hafnium (IV) oxide as a biocompatible passivation layer for biological LOCs due to its relatively high dielectric constant [22] and optically transparency [28].

1.3. Hafnium oxide

Advantageous properties of hafnium oxide (HfO_2) include its chemical stability, high dielectric constant (20–25), wide band gap (5.8 eV), conduction band offset (1.4 eV), optical transparency from 300 to 10,000 nm in the electromagnetic spectrum, and refractive index (~2) based on deposition conditions [22, 28–30]. These properties prompted HfO_2 use in gate oxide in metal–oxide–semiconductor field-effect transistors (MOSFET) [18, 19, 28–35] whereby SiO_2 is unsuitable due to scaling limitations [19]. Other common HfO_2 uses include optical coatings [19, 29, 30, 33], optoelectronics [19, 28, 30], and ceramics [28, 30]. This substantial foundation of electrical and optical knowledge is advantageous to build upon for LOC applications.

Hafnium oxide's utilization for biological applications is increasing, especially within nanopore and nanowire structures. HfO_2 increased the sensitivity of silicon-based multi-nanowires for DNA and protein detection due to its chemical stability, pH sensitivity, high dielectric constant, hydrophilicity, and isoelectric point of 7 [20, 37–40]. HfO_2 demonstrated stability within an aqueous electrolyte environment and was successfully functionalized with biotin biomolecule probes when used as a gate dielectric for charge based biosensors [20]. Hafnium oxide pH responses (51.0–55.8 mV/pH) [36] were comparable to other Si nanowire, Al_2O_3/SiO_2 pH sensors (54.9–60.2 mV/pH) [41] when investigated for ion sensitive field effect transistors (ISFET) and MOSFETs. Table 1 summarizes biological applications that utilized HfO_2 along with deposition methods, characterization methods, and substrates. In this paper, fabrication and multi-dimensional characterizations of HfO_2 films needed for LOC technologies are presented with a particular emphasis on concurrent optical and electrokinetic cell characterizations.

1.4. Deposition and characterization of hafnium oxide

Optical and electrical properties of HfO_2 are affected by crystallography, microstructure, integral stoichiometry, binding states, morphology, contamination, and defect density [29], making HfO_2 deposition important. For very thin films, industry typically uses atomic layer deposition (ALD) [18]. Other deposition methods include organic vapor deposition [42], metal-organic vapor deposition [18], electron-beam evaporation, reactive vacuum evaporation [33], and a variety of sputtering techniques [19, 21, 28–30, 34]. Herein, RF sputtering was used for all HfO_2 film depositions.

Deposition parameters affecting HfO_2 film properties include temperature, pressure, voltage, plasma composition, and annealing [19, 21, 33]. Tables 2 and 3 contain the deposition methods, characterization methods, and substrates used to determine HfO_2 characteristics/quality for non-sputter (Table 2) and sputter deposition techniques (Table 3). Characterization methods include spectroscopic ellipsometry (SE),

Table 2
Non-sputter deposition techniques and HfO_2 characterization.

Ref.	Deposition method	HfO_2 (nm)	Substrate	Deposition parameters	Characterization methods
[40]	ALD	16	Graphene/TiO_2 and Si, p-type, highly doped	Annealing temperature (none, 500–700 °C)	FFT, Contact angle, IV, Leakage current, TEM
[18]	ALD MO-CVD	< 7	Si and Si covered with SiO_2	Study of possibilities and limitations of near UV–visible range SE	*SE,* AR-XPS, RBS
[42]	MO-CVD	4	Si, p-type	Estimation of dielectric density	*SE,* XRR
[33]	Reactive vacuum evap.	~75–170	Si, single-crystal	Deposition temperature (40–280 °C)	*SE, AFM, XRD*

scanning electron microscopy (SEM), and Fourier transform infrared spectroscopy (FTIR) for thickness; atomic force microscopy (AFM), X-ray diffraction (XRD), energy dispersive X-ray spectroscopy (EDS), X-ray photoelectron spectroscopy (XPS), and X-ray reflectometry (XRR), for structural properties; SE, FTIR, and ultraviolet-visible spectroscopy (UV–VIS) for optical properties; and SE, capacitance-voltage (CV), and current-voltage (IV) for electrical properties, among others including grazing incidence X-ray diffraction (GIXRD), angle-resolved X-ray photoelectron spectroscopy (AR-XPS), Rutherford backscattering spectroscopy (RBS), Doppler broadening spectroscopy (DBS), transmission electron microscopy (TEM), fast Fourier transform (FFT), and fluorescence interference contrast (FLIC).

To expand knowledge of HfO_2 performance for biological LOC technologies, this work explored HfO_2 deposition and characterization for isolating electrodes from aqueous, biological samples. Three HfO_2 thicknesses were sputter deposited on both opaque silicon and transparent glass substrates. HfO_2 characterizations included AFM, XRD, energy dispersive X-ray spectroscopy field emission scanning electron microscopy (EDS-FESEM), and FTIR characterizations for structural properties; SE for thickness and optical properties; and SE, CV, and simulations for electrical properties. In addition, this study explored HfO_2 biocompatibility with cells. These results have implications in biological LOC devices that use optical measurement methods concurrent with electrode isolation.

2. Materials & methods

2.1. Hafnium oxide deposition

Hafnium oxide thin films were deposited on four types of substrates: 500 µm thick (100) oriented single side polished (SSP) and 500 µm thick double side polished (DSP) 10 Ω-cm resistivity silicon wafers, 75 × 25 × 1 ± 0.1 mm soda lime glass microscope slides, and 500 µm thick Borofloat 33 borosilicate glass wafers (UniversityWafer.com). The latter two were optically transparent and utilized for many LOC devices [43]. HfO_2 RF sputter deposition (Perkin-Elmer 2400-8J, Waltham, MA) progressed at room temperature with an RF power of 700 W, a 99.95% pure hafnium target (Kurt J. Lesker, Jefferson Hills, PA), and base and operating pressures of 2.7×10^{-4} to 4.0×10^{-4} Pa and 0.93–1.02 Pa, respectively. Film stoichiometry was maintained using 4 SCCM O_2 and 18 SCCM Ar and was characterized in Section 3.3. Films were treated as HfO_x until film stoichiometry was confirmed. Depositions ran for 6.5, 13, and 20 min with an average deposition rate of 12 nm/min, as determined by ellipsometry calibration of HfO_2

Table 3
Sputter deposition parameters and HfO_2 characterization.

Ref.	HfO_2 (nm)	Deposition	Substrate	O_2 and Ar flow	RF (W)	T (°C)	BP (Pa) DP (Pa)	DT (min)	CM
[a,b]	78, 156, 240	RF	SSP DSP Glass	4 SCCM O_2 18 SCCM Ar	700	Room	2.7×10^{-4} to 4.0×10^{-4} 0.93–1.02	6.5, 13, 20	*AFM, XRD, EDS-FESEM, FTIR, SE, CV*
[32][b]	67.6, 86.3, 104, 128.9	RF magnetron	Si (001) 2–5 Ω/cm Quartz	20 SCCM Ar	50, 60, 70, 80	Room	$> 2.0 \times 10^{-4}$ 0.35	120	*AFM, XRD, FTIR,* UV–Vis, *SE*
[19][c]	33.19 to 35.38	RF magnetron	Si (100) p-type 4–7 Ω/cm	–	–	–	1.5×10^{-3} 2.2	7	*AFM, FTIR,* IV, *SE, CV*
[21][d]	7.8 to 71.6	RF magnetron	Si (100) p-type 1–10 Ωcm	5, 10, 15 ml/min O_2	100, 300, 500	–	– 0.4, 0.8, 1.2	2, 5, 10	*AFM, XRD,* IV, RBS, *CV*
[28][b]	40	RF magnetron	Si (100)	12 SCCM O_2 28 SCCM Ar	100	Room to 700	1.3×10^{-3} –	–	GIXRD, XRR, *SE*
[29][b]	–	Magnetron	Si (100) n-type	30 SCCM total $O_2/(O_2 + Ar)$ ratio (0.07, 0.26, 0.59)	25, 45, 100	–	2.0×10^{-3} 0.7, 1.0, 4.0	–	*XRD,* DBS, *SE*
[30][b]	~95 to 155	RF magnetron (reactive)	Si (100)	0, 0.1, 0.2, 0.3, 0.4 $O_2/(Ar + O_2)$	100	300	1.3×10^{-3} –	45	*XRD, SEM, SE*
[31][b,e]	7.3	DC magnetron	Si (100) p-type 7–17 Ωcm	12 SCCM O_2 30 SCCM Ar	30	200	$< 2.7 \times 10^{-3}$ 5.9×10^{-2}	5	*XRD, FTIR,* XPS, *SE*
[34][b,f]	–	Reactive w/pulsed DC power	Si	10 SCCM O_2 28.3 SCCM Ar	42	–	2×10^{-3} 1	60	DBS, XRR, *SE*

[a] This paper T = Temperature, BP = Base Pressure, DP = Deposition Temperature, DT = Deposition Time, CM = Characterization Methods.
[b] Papers that reported the target used: all ≥99.9% hafnium oxide or hafnium metal target.
[c] Annealing temp. 350, 550, 750 °C.
[d] Annealing temp. 300, 600, 900 °C.
[e] Study of SiO_x formation at HfO_2/Si interface.
[f] 40 kHz pulse, 70% duty factor, study of atomic O_2 treatment.

deposited on silicon. For each deposition time, Si and glass substrates were sputtered together to enable direct comparisons.

Surface cleaning processes used in LOC fabrication were compared in Section 3.1 by cleaving HfO_2 coated substrates into three pieces: as-deposited control, oxygen plasma treatment, and Piranha treatment. The oxygen plasma treatment was performed via RIE at 3.2×10^4 Pa for 40 s (Jupiter II, March Instruments, Concord, CA). The Piranha treatment was performed by soaking substrates in Piranha solution, a strong corrosive oxidizing agent prepared by mixing 12 N H_2SO_4 and 30% H_2O_2 (1:1 v/v) (Sigma Aldrich, St. Louis, MO), for 5 min, rinsing with deionized water, and drying with nitrogen gas.

2.2. Hafnium oxide characterization

2.2.1. Atomic force microscopy

Structural properties and morphology of the HfO_2 films were examined on both DSP silicon and soda lime glass substrates, with pre- and post-oxygen plasma and Piranha treatments. A Veeco Dim 3000 atomic force microscope (Plainview, NY) in tapping mode at 1 Hz was utilized to scan areas of $5 \times 5\,\mu m^2$ with a resolution of 103 pixels per micron. Nanoscope V530 software collected data and measured surface roughness. Grain size analysis was conducted with Image-J software (NIH, https://imagej.nih.gov/ij/). The minimum and maximum pixel area threshold sizes were systematically adjusted on the B&W images to identify both grains and grain agglomerates from the background, 100 to 1000 pixels squared and 100 to infinity pixels squared, respectively. Data was compiled and compared across treatments, substrates, and film thicknesses. The size of the grains, along with roughness and surface morphology revealed film growth conditions and the impact of oxygen plasma and Piranha treatments.

2.2.2. X-Ray diffraction

Because the film crystal structure and size can affect the film's optical and electric properties, the bulk morphology of the deposited HfO_2 was further explored with XRD for different deposition times on SSP silicon and soda lime glass substrates. XRD was used in a glancing angle mode to obtain crystalline structure as a function of film thickness. A 2θ scan was performed from 18 to 67.98°, using a 2000 W Cu target X-ray tube on a Scintag XDS-2000 θ/θ powder diffractometer (CA, USA). The X-ray tube utilized Cu Kα1 radiation (wavelength: 1.540562 Å) and a tungsten filament. The step scan mode was used with a scan rate of 0.003°/min. The Scherrer equation was employed to relate crystallite size in the deposited films to the broadening of a peak in the diffraction pattern. The mean size of the crystallites (τ) was calculated using $\tau = K\lambda/\beta cos\theta$, with K as a dimensionless shape factor, λ as the X-ray wavelength, β as half the maximum intensity in radians, and θ as the Bragg angle. The dimensionless shape factor utilized was 0.9, because values range from 0.86 to 0.94 depending on crystallite's circular to cubic shape, respectively [44]. The Cu tube on the system yielded an X-ray wavelength of 0.154056 nm, which is the characteristic wavelength for K-alpha radiation [45].

2.2.3. Energy dispersive X-Ray spectroscopy and Fourier transform infrared spectroscopy

Film thickness, morphology, and composition were measured via field emission scanning electron microscopy (FE-SEM, Hitachi S-4700, Tarrytown, NY) at 20 keV and 200 k magnification. A sputtered carbon coating on the HfO_2 films prevented charging to obtain higher quality images. Morphology comparisons were made between AFM and SEM. To gain insights to compliment morphology and crystalline structure, the film composition was analyzed via SEM-EDS and FTIR. Films on DSP silicon and soda lime glass were analyzed with deposition times of 13 and 20 min, respectively. In addition, the 20-min deposition on DSP silicon was scanned, and a thickness comparison was made between the SEM and ellipsometry results. To achieve a cross-sectional analysis and thus discern thickness, the HfO_2 coated silicon wafer was cleaved and mounted on a holder perpendicular to the electron beam. EDS composition was compared to FTIR by scanning the DSP silicon film (Genesis II, Mattson Instruments, Madison, WI) from 400 to 4000 cm^{-1}. Silicon background peaks were removed. SEM-EDS and FTIR both corroborated stoichiometric HfO_2.

2.2.4. Spectroscopic ellipsometry

Thickness and optical characterizations were completed via spectroscopic ellipsometry for all deposition times and substrates. Each film was scanned across 400 to 1000 nm wavelengths at angles of 65°, 70°, and 75° to measure the ellipsometric parameters psi (ψ) and delta (Δ) (JA Woollam V-VASE, Lincoln, NE). Material models were fitted to the collected data, and a regression analysis was used to find the mean square error (MSE). Minimizing the MSE was the criteria used to select optimal material models. The films were modeled as Lorentz-Tauc Oscillators, which considered the bandgap [46] and included a 10 nm SiO_2 layer. The model required surface roughness which was obtained via AFM, presented in Section 3.1. The WVASE32 software used ψ and Δ models to predict film thickness, refractive index, and extinction coefficient, from which the optical properties of the deposited films were assessed.

2.2.5. Capacitance-voltage

Capacitance-voltage measurements were used to extract the film dielectric constant. Experiments were conducted using a series of 1000–2000 μm circles that had an Al/HfO_2 (6.5-min deposition)/Al configuration, as shown in Fig. 5. A HfO_2 film was sputtered on an Al (100 nm) coated SiO_2/Si wafer, with a portion protected with a glass slide to allow for probing to the underlying Al film, followed by a 100 nm Al film deposited through a shadow mask. The shadow mask had 1000, 1500, and 2000 μm diameter circles. Due to the step change, the thickness of the Al and HfO_2 films were measured with a 3D profilometer (Filmetrics Profilm3D, San Diego, CA). CV measurements were collected using an HP 4284A Precision LCR Meter (Agilent, Santa Clara, CA) by connecting to the underlying and top Al films. Capacitance values were converted to the dielectric constant using $C = A(\kappa/d)$, with C as the measured capacitance, A as the area of the capacitor (e.g., each respective circle), κ as the dielectric constant of the insulator, and d as the separation of the two Al films.

2.2.6. Simulations

Along with the determination of the dielectric constant of the HfO_2 films, COMSOL Multiphysics (Burlington, MA, USA) simulation software was used to model HfO_2 electrical isolation of the electrodes from the fluidic layer. Electric potential distributions in a 2D geometry were obtained by solving Laplace's equation using the Lagrange element method. The 2D model geometry, shown in Fig. 6a, consisted of a $200 \times 40\,\mu m$ substrate, two $20 \times 0.15\,\mu m$ Au electrodes (excitation and ground), HfO_2 passivation with targeted thicknesses (0.078, 0.156, and 0.240 μm) over the substrate and electrodes, in contact with a $200 \times 70\,\mu m$ chamber filled with 0.1 S/m phosphate buffer saline (PBS) fluidic layer. Material properties utilized are shown in Table 4. Boundary conditions were *Electric Potential* (5 V) from the Au excitation electrode, *Ground* at the Au ground electrode, and *Electrical Insulation* at all outer boundaries. To evaluate the electric potential distribution, the

Table 4
Material properties and parameters employed for electric potential simulations.

Material	Relative ε	σ [S/m]
Borosilicate glass	4.5	1×10^{-15}
Silicon	11.7	0
Hafnium Oxide	20.32[a]	1×10^{-16}
Water	80	0.1

[a] Value obtained from CV measurements, Section 3.5

simulated was run between 10 Hz and 10 MHz with a mesh consisting of elements ranging from 0.004 to 2 μm.

2.2.7. Biocompatibility

In addition to physical, optical, and electrical properties, the deposited film biocompatibility was investigated. Healthy red blood cells (RBCs) were contacted with HfO_2 films, and the extent of hemolysis was determined by measuring the absorbance of free hemoglobin according to standards by Xiong et al. [47, 48]. Whole blood was drawn from a healthy, anonymous consenting donor via IRB approved protocols into ethylenediaminetetraacetic acid (EDTA) Becton Dickinson vacutainers (MTU IRB M0540[318164-11]). Blood was centrifuged at 132 relative centrifugal force (rcf) for 10 min to separate into platelet-rich plasma, white blood cells, and packed RBCs. Packed RBCs were re-suspended and diluted in sterile, isotonic 0.9 w/v% NaCl to a 1:100 ratio for the hemolysis assay. A 4″ borosilicate glass wafer coated with HfO_2 was diced into 20 × 20 mm pieces and separately submerged into 50 ml tubes containing the 1:100 RBC suspension, then incubated at 37 °C for 1, 3, and 5 h. A negative control of the 1:100 RBC suspension was conducted without HfO_2. A positive control (100% lysis expected) was conducted with the 1:100 RBC suspension incubated with 1 w/v% Triton X-100 and without HfO_2. All conditions were concurrently conducted in triplicate. After incubation, RBC suspensions were centrifuged at 1075 rcf for 10 min and the supernatant collected. Free hemoglobin absorbance readings were obtained via UV/Vis spectrophotometry (Genesis 10 UV Scanning, Thermo Fisher Scientific, Waltham, MA) at 380, 415, and 450 nm, corresponding to the hemoglobin peaks [47]. A 0.9 w/v% NaCl blank control was measured to calculate the corrected absorbance of free hemoglobin ($Ab_{free\ hemoglobin}$) (Eq. (1)) and percent hemolysis was obtained relative to the 100% hemolysis positive control to compare across exposure conditions (Eq. (2)). Materials were deemed biocompatible if hemolysis was negligible [47].

$$Ab_{free\ hemoglobin} = 2 \times A_{415} - (A_{380} + A_{450}) \quad (1)$$

$$\%hemolysis = \frac{Ab_{free\ hemoglobin}\ of\ test\ sample}{Ab_{free\ hemoblobin}\ of\ positive\ control} \times 100\% \quad (2)$$

3. Results & discussion

Diverse characterization techniques were utilized to investigate the effectiveness of hafnium oxide properties as a passivation layer for biological LOC devices. Morphology/crystallinity was measured and compared via AFM and XRD. Composition was measured and compared via SEM-EDS and FTIR. FTIR results were also used to determine potential optical interferences from HfO_2. Measurements, except FTIR, were compared between crystalline silicon and amorphous glass substrates. Film thickness was measured via ellipsometry and SEM. Ellipsometry also provided optical properties including refractive index and extinction coefficient. Dielectric constant measurements were completed via CV. COMSOL simulations utilized these properties to explore the electrical passivation capabilities of the HfO_2 films. In addition to the physical, optical, and electrical properties, HfO_2 film biocompatibility was studied via hemolysis.

3.1. Atomic force microscopy

Surface morphology of the deposited HfO_2 was studied via AFM. Topographical images for three HfO_2 film thicknesses are shown in Fig. 1, organized by columns to compare as-prepared films to piranha-treated films with rows organized to allow comparisons between DSP silicon and soda lime glass substrates as well as film thickness. Oxygen plasma and piranha treatments were employed to ascertain the impact of an oxidizing agent on film surface morphology. The oxygen plasma

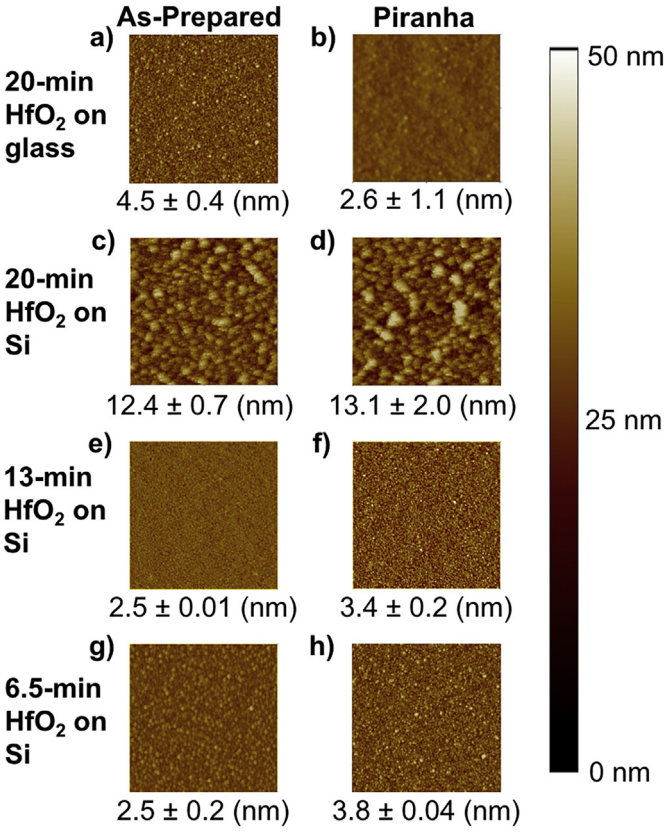

Fig. 1. AFM images of three different HfO_2 thicknesses deposited on soda lime glass (a–b) and DSP silicon (c–h) substrates before and after a 5-min Piranha treatment. The substrate utilized effected grain size with the thickest, 20-min deposition films on glass showing comparable grain size to that of the thinner films on silicon. Piranha treatment changed surface roughness of the 20-min deposition on glass, but not of the 20-min deposition on silicon.

treatment showed no discernible change and thus is not shown. Piranha treatment smoothed the glass/HfO_2 surfaces as shown in and b, but no significant changes were observed for Si/HfO_2 surfaces with different thicknesses.

For the 20-min HfO_2 depositions, roughness (RMS) on the silicon substrate was 12.4 ± 0.7 nm as compared to 4.5 ± 0.4 nm on the glass. Comparable literature values for RMS roughness increased from 5 to 12 nm for 13-min depositions on silicon films with increasing substrate temperatures from 25 °C to 120 °C [49]. Generally, as the grain size increased, the roughness increased. Fig. 1c, e, and g illustrate that as the HfO_2 thickness increased on silicon, agglomeration at the grain boundaries occurred. Such grain agglomeration could be due to temperature effects during HfO_2 deposition [50–52] because, with longer deposition times, the substrate heated up due to free energy losses in the system. Interestingly, the grain size of the thinnest, 6.5 and 13-min, HfO_2 films on the molecularly ordered silicon resembled that of the thickest, 20-min, HfO_2 on the molecularly disordered glass. The secondary grain size analysis using Image-J confirmed that the HfO_2 molecules organized into smaller grains on glass than on silicon, and demonstrated that there were fewer grain boundaries in the HfO_2 film on the silicon.

3.2. X-Ray diffraction

X-ray diffraction was used to expand the grain analysis investigating the crystalline structure of the HfO_2 films. Fig. 2 shows the effect of HfO_2 deposition time, and thus thickness, on the XRD pattern for SSP

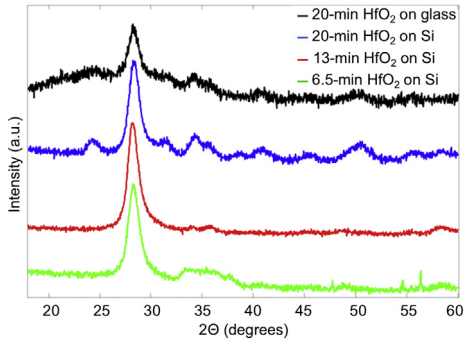

Fig. 2. XRD pattern for 6.5, 13, and 20-min depositions on SSP silicon and a 20-min deposition on soda lime glass. All spectra exhibit the characteristics peak of (111) plane at 28.47°; however, as the thickness of the HfO_2 film increases more peaks appear in the XRD spectra suggesting crystallite growth in multiple planes demonstrating the tendency for HfO_2 to grow along different planes.

silicon and soda lime glass substrates. All HfO_2 films exhibited the characteristic peak for the (111) plane at 28.47°. For the 6.5-min deposition of HfO_2 on silicon, there was a broad peak from 32.22 to 38.91° which suggested a (200) orientation. Narrow peaks at 47.22, 54.56, 55.4, 56.33, and 65.87° were attributed to stray atoms from the energized tungsten filament, which were attracted to the water-cooled copper target and emit tungsten radiation [53].

As the film thickness increased on silicon, more planes were observed. Both the 13 and 20-min depositions showed peaks (34.21° and 35.7°) corresponding to the (200) plane, and the 20-min deposition showed an additional peak (50.8°) corresponding to the (220) plane. There was preferred growth along the (111) plane, as demonstrated by the dominance of the (111) peak at 28.47°. The presence of additional peaks for longer depositions showed HfO_2 growth along different planes. The thickest layer of HfO_2 on glass had a similar result as the thinnest layer of HfO_2 on silicon and was consistent with literature [54, 55]. Based on the Scherrer equation, crystallites from the 6.5, 13, and 20-min HfO_2 depositions on silicon were calculated to be 2.9, 2.6, and 4.1 nm while the 20-min HfO_2 deposition on glass was 3.8 nm.

HfO_2 roughness and crystallite size differed between glass and silicon. The XRD results for the 20-min deposition on glass and the 6.5-min deposition on silicon yielded the same orientation of (111) with roughness and crystallite size 78% and 81% greater on glass than on silicon, respectively. For the same film thickness (20-min depositions), the roughness was 64% smaller, and the crystallite size was 11% smaller for the glass than the silicon. These results suggested the structured silicon, when compared to the amorphous glass, supported larger HfO_2 crystallite formation. As the film thickness increased, not only did the grain size increase, as demonstrated by the AFM results, but there was also a trend of increasing crystalline domain size.

3.3. Energy dispersive X-ray spectroscopy and Fourier transform infrared spectroscopy

Once grain size was determined, energy dispersive X-ray spectroscopy was done at both 20 kV and 5 kV to determine the composition of two HfO_2 films: 13-min on DSP silicon and 20-min on soda lime glass. Fig. 3a shows the EDS spectra using a 20 kV acceleration voltage that penetrated the HfO_2 film resulting in a small substrate signal; oxygen and hafnium dominated the spectra. For the silicon substrate, oxygen, hafnium, and carbon peaks were apparent; carbon originated from the carbon coating sputtered to enable imaging. For glass, the same oxygen, hafnium, and carbon peaks were observed along with nickel, sodium, calcium, and silicon peaks attributed to the soda-lime glass slide composition [56]. An accelerating voltage of 5 kV was employed to minimize contributions from the substrate; the atomic percent for oxygen and hafnium were 66.92% and 33.08%, respectively, confirming that the films were 99% stoichiometric HfO_2 for a penetration depth of ~250 nm. The cross-sectional analysis of the 20-min deposition showed an HfO_2 layer 180–230 nm thick, on top of a thin layer of SiO_2, as shown in Fig. 4c.

Films were also scanned using FTIR to investigate composition. No peaks were observed at wavenumbers > 1300 cm^{-1}; therefore the data was truncated to 400–1300 cm^{-1} as shown in Fig. 3b. The sharp peak at 670 cm^{-1} was a C—O chemical bond resulting from measuring in ambient air. The peak at 610 cm^{-1} was due to silicon phonon absorption [57, 58]. The peak at 1050 cm^{-1} was attributed to the Si-HfO_2 interface where a $HfSi_xO_y$ composite was formed [31, 58]. Peaks at 748 cm^{-1}, 512 cm^{-1}, and 412 cm^{-1} were related to the HfO_2 film. The first peak was HfO_2, while the latter two were Hf—O chemical bonds [31, 57, 58]. This agreed with the EDS results demonstrating that the deposited films were stoichiometric HfO_2. The peak locations not only indicated composition, but they also inferred that there is optical interference at those wavelengths. This information can inform experimental designs in optical lab-on-a-chip systems to exclude wavelengths with HfO_2 interference.

3.4. Spectroscopic ellipsometry

Spectroscopic ellipsometry measurements included inference of each deposited HfO_2 film thickness from silicon and glass model fits as well as refractive index and extinction coefficient as shown in Fig. 4 and Table 5. Fig. 4 illustrates a representative experimental data set with an angle 70° and the fitted model for psi (ψ) and delta (Δ) as a function of wavelength for three HfO_2 thicknesses. Glass substrate transparency did not allow standard reflection measurements, instead lower accuracy transmission measurements were performed. MSE values indicated that glass yielded unreliable data, caused by refractive index similarities between HfO_2 and glass. SE was not the optimal tool for characterizing HfO_2 on glass, and thus glass ellipsometry results are not presented

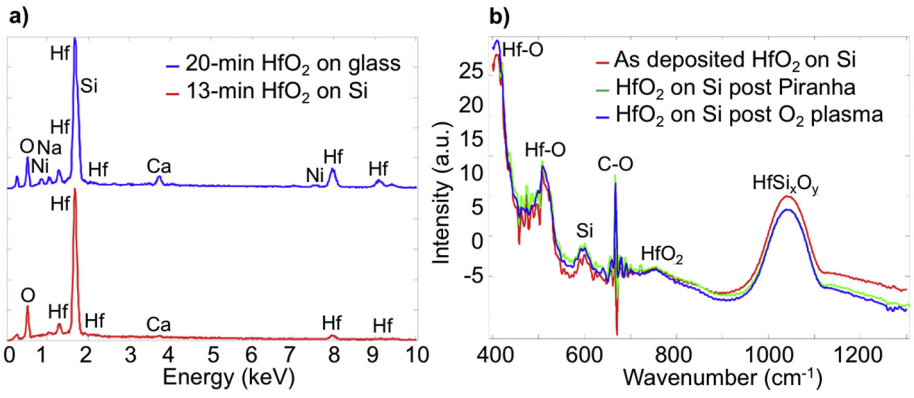

Fig. 3. a) EDS analysis at 20 kV of the 13-min HfO_2 film on DSP silicon and the 20-min HfO_2 film on soda lime glass confirming stoichiometric deposition for HfO_2. b) Transmission mode FTIR analysis of the HfO_2 deposited on a 20 Ωcm DSP silicon wafer as prepared and after oxygen plasma and Piranha treatments. FTIR corroborates that the deposited films are stoichiometric HfO_2.

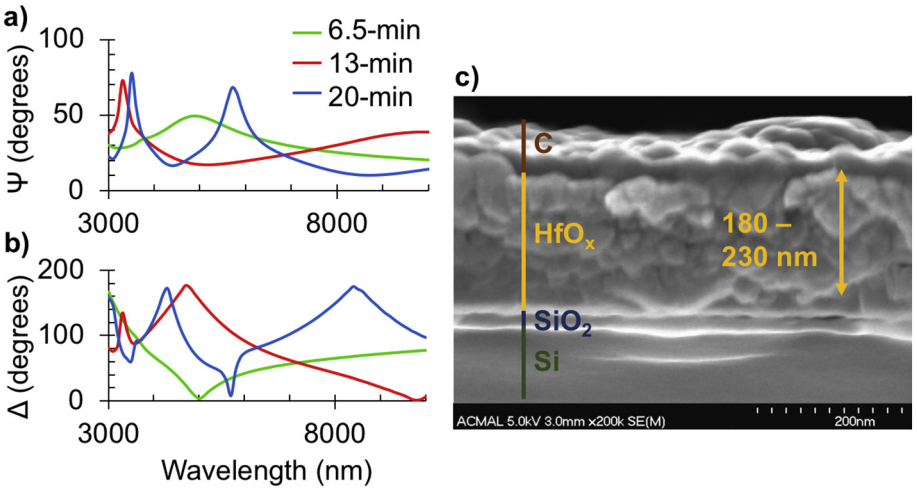

Fig. 4. Ellipsometry a) psi and b) delta waves for an angle of 70° for HfO_2 measured on silicon for all three deposition times: 6.5, 13, and 20-min yielding 58, 127, and 239 nm thicknesses with MSEs of 0.5411, 52, and 7.727, respectively. Measurements were conducted for all three deposition times on silicon and glass and were used to determine thickness, refractive index, and extinction coefficient. (b) Cross-sectional SEM image showing the silicon substrate, SiO_2 interfacial layer, HfO_2 film, and the carbon over layer used for data collection for a 20-min deposition of HfO_2. Results show a HfO_2 film of 180–230 nm based on the location.

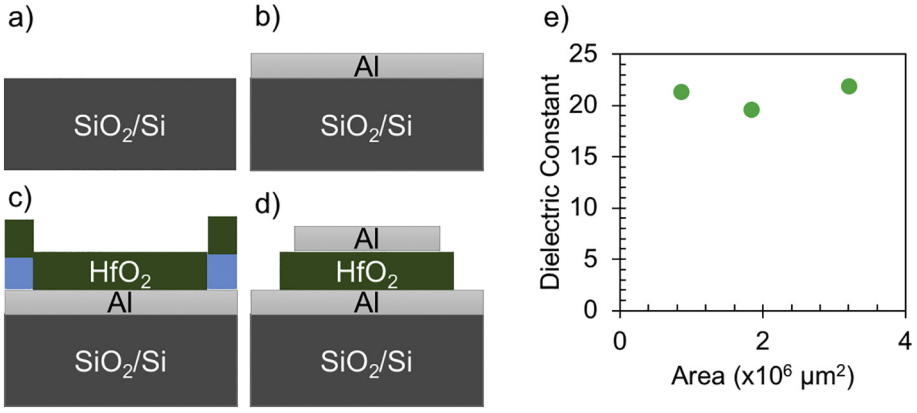

Fig. 5. a–d) Microfabrication of 1000–2000 μm diameter, sandwiched (100/72/100 nm) Al/HfO_2/Al pattern used for CV measurements. e) Dielectric constant as a function of area for a 6.5-min HfO_2 deposition. The average dielectric constant of 20.3 ± 1.55 is consistent with literature values for HfO_2.

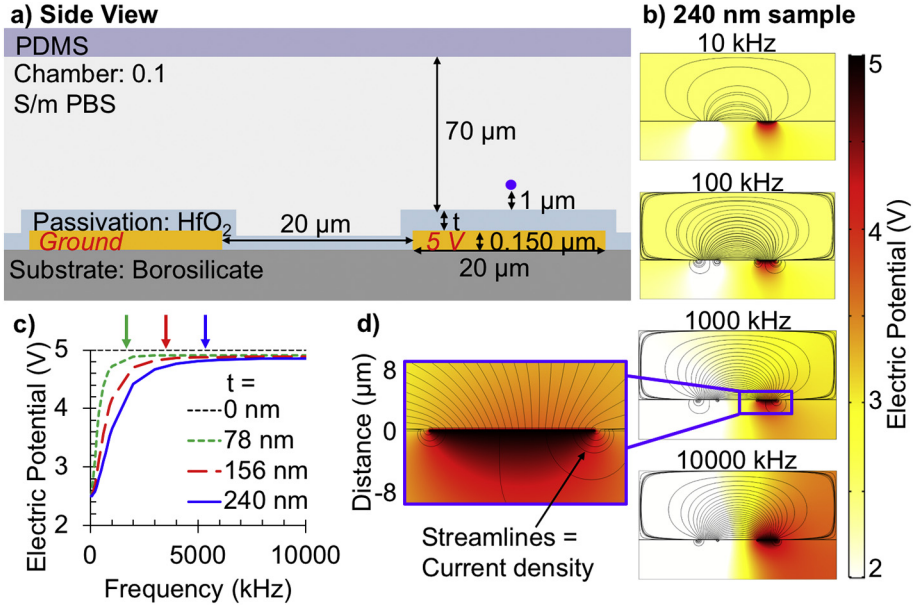

Fig. 6. a) 2D geometry used for COMSOL simulations with 200 × 40 μm substrate, two 20 × 0.15 μm Au electrodes (excitation and ground), HfO_2 thickness (t = 78, 156, and 240 nm) over the substrate and electrodes, in contact with a 200 × 70 μm 0.1 S/m PBS fluidic layer. b) Electric potential distribution (surface plot) and current density (streamlines) for the 240 nm thick HfO_2 passivation layer at frequencies of 10, 100, 1000, and 10,000 kHz. c) Magnitude of the electric potential that penetrated through the passivation layer into the chamber at a height of 1 μm above the working electrode (purple dot in a) as a function of frequency and film thickness. Arrows correspond to the frequency threshold whereby the maximum potential of ~4.85 V was reached. d) Close up of working electrode at a frequency of 1000 kHz. Results demonstrate that HfO_2 allowed electric field penetration into the fluidic layer while preventing direct physical contact between electrodes and fluidic layer. (For interpretation of the references to color in this figure legend, the reader is referred to the web version of this article.)

herein. HfO_2 was deposited on glass and silicon in the same chamber run, so thicknesses measured on silicon were inferred for the respective films on glass.

The MSE values for the 6.5 and 20-min depositions on silicon indicated good model fits [59]. The Cauchy dispersion relationship, which assumed isotropic material, was used as the primary model and the thinnest film followed the trend of previously published data [28]. Model deviations and higher MSE values were obtained for the 13 and 20-min depositions, suggesting that the increasing thickness increased the anisotropy of the films. This agreed with the XRD results presented

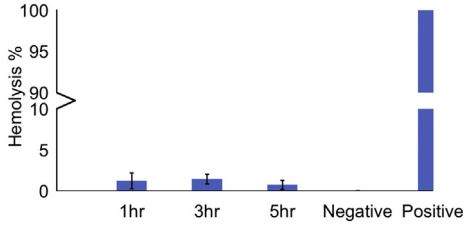

Fig. 7. RBC hemolysis after 1, 3, and 5 h of exposure to borosilicate glass coated with HfO_2, as well as, negative (no HfO_2), and positive (1 w/v% Triton X-100) controls. This demonstrated that HfO_2 is a suitable material for passivating electrodes within biological LOC devices that use cells.

Table 5
Ellipsometry results for different HfO_2 deposition times.

Deposition time (min)	6.5	13	20
Targeted thickness (nm)	78	156	240
Thickness (nm)	58	127	239
Mean square error	0.5411	52	7.727
Refractive index	2.03 ± 0.02	1.99 ± 0.03	1.82 ± 0.01
Extinction coefficient	0.002 ± 0.002	0.004 ± 0.004	0.006 ± 0.009

in Section 3.2, which also showed HfO_2 anisotropy. A more complex model may be able to account for anisotropy in the thicker deposited HfO_2 films [59, 60] and increase accuracy.

Both the 13 and 20-min depositions contained a characteristic ψ absorption peak around 3400 nm. The 20-min deposition contained an addition ψ peak around 5700 nm, which indicated another resonance mode due to the thicker film thickness. The thickness inferred from the ellipsometry model was highly consistent with instrument calibration for the 20-min deposition. The cross-sectional SEM image in Fig. 4c illustrates spatial variations in film thickness from 180 to 230 nm for HfO_2 and 20 nm for SiO_2; this thickness was fairly consistent with the ellipsometry results of 239 nm.

As shown in Table 5, SE modeled refractive index (n) for wavelengths from 400 nm to 1000 nm and varied around 2, consistent with literature [28, 33]. Refractive index profiles for each film thickness were not identical as a function of wavelength due to the increasing anisotropy with thickness. Lastly, the extinction coefficient was close to zero, which was expected for a transparent material and was consistent with previously reported data [61].

3.5. Capacitance-voltage

Capacitive measurements were collected at 100 kHz for applied potentials from -5 V to 5 V. However, due to the thickness, the HfO_2 films could not be fully depleted, and therefore no modulation was observed. Fig. 5a–d depicts fabrication for the utilized Al/HfO_2/Al configuration. The thicknesses of the Al and HfO_2 films were 100 nm for the Al and 72 nm for the 6.5-min HfO_2 deposition– fairly consistent with the 78 nm thickness interpolated from the deposition calibration. The dielectric constant was calculated from the measured capacitance, per the equation $C = A(\kappa/d)$, as a function of HfO_2 area as shown in Fig. 5e. For the 1000–2000 μm diameter circles, the dielectric constant ranged from 18.0 to 23.6, with an average of 20.3 ± 1.55, consistent with 20–25 reported in the literature [22].

3.6. Simulations

Once HfO_2 material properties were determined, AC electrostatics simulations were used to investigate the electrical passivation of different thicknesses of HfO_2 over frequencies from 10 to 10,000 kHz. Simulations were performed for both silicon and borosilicate glass substrates, but these substrates did not significantly affect dielectric performance (the difference between silicon and glass ranged from 1.172×10^{-5} to 1.179×10^{-3} V) or electric potential profiles. Fig. 6a shows the 2D geometry modeled over borosilicate comprised of a 20 μm fluidic span between two 20 μm electrodes, all uniformly passivated with 78, 156, or 240 nm of HfO_2. Fig. 6b shows color maps of the chamber's electric potential distributions for 240 nm of HfO_2 as a function of frequency, while Fig. 6c illustrates dependence on both frequency and film thickness at a location 1 μm above the working electrode. For all thicknesses, a potential of 5 V was applied at the working electrode and 0 V at the ground electrode to then observe heat maps of the current between the working and ground electrodes through the fluidic chamber. Simulations illustrated that HfO_2 allowed electric field penetration into the fluidic layer while preventing direct physical contact of the fluidic layer with the electrodes, thus preventing unwanted side reactions and electrode fouling. Potential leakage within the substrate resulted from the dielectric nature of borosilicate whereby no charge flowed, as indicated by the lack of current density streamlines.

For all cases, the electric field penetrated the passivation layer yet varied with HfO_2 thickness and frequency. At frequencies below 10 kHz, HfO_2 suppressed half of the applied electric potential regardless of thickness. A similar but opposite behavior was observed at frequencies > 10 MHz, at which a potential of 4.85 V was reached regardless of the thickness. This confirmed that the capacitive coupling through the HfO_2 film was higher at higher frequencies. The frequency at which the HfO_2 film became nearly electrically transparent, with a potential of 4.85 V in the fluidic layer, was dependent on thickness. The arrows in Fig. 6c demonstrate this threshold for each film thickness. Simulations provide a foundation of electrical passivation characteristics of the HfO_2 for different thicknesses and different AC frequencies; this simulation framework may be useful for design and parameter optimizations for specific operating conditions or applications, such as constant current for field gradients.

3.7. Biocompatibility

HfO_2 film hemocompatibility was evaluated by exposing red blood cells in an isotonic 0.9 w/v% NaCl solution to a 20 × 20 mm borosilicate glass substrate coated with HfO_2 for up to 5 h and measuring the amount of free hemoglobin in the supernatant after centrifugation. Fig. 7 shows the percent hemolysis results for RBCs after 1, 3, and 5 h of incubation at 37 °C with HfO_2, along with the negative (no substrate or HfO_2) and positive (1% w/v Triton X-100 surfactant) controls completed in triplicate. Hemolysis varied between 0.75% and 1.45% when exposed to the HfO_2 without an apparent trend with exposure time. The negative control not exposed to HfO_2 showed 0.06% hemolysis, while the positive control showed 100% hemolysis. These results illustrated that HfO_2 was compatible with RBCs and is suitable as a passivation layer on lab-on-a-chip devices using blood as a primary sample.

4. Conclusions

Sputter-deposited hafnium oxide films of three different deposition times, 6.5, 13, and 20-min, were fabricated and characterized for use as a passivation layer in a biological electrokinetic microdevice system requiring sufficient optical transparency, electrode isolation, and biocompatibility. EDS and FTIR both confirmed that the composition of the films were stoichiometric HfO_2. Film structural properties were explored via AFM, XRD, EDS, and FTIR. AFM results show surface roughness depended upon the substrate, with 64% smaller grain sizes and 11% smaller crystallite size on amorphous glass than silicon for the same 20-min deposition. Surface roughness increased with deposition time from 5 nm to 12 nm on silicon. XRD results agreed with AFM results, showing an increase in crystallite size from 0.844 to 1.19 nm, with increasing deposition time. The XRD results for the 20-min deposition on glass and the 6.5-min deposition on silicon yielded the same orientation of (111) with roughness and crystallite size 78% and 81%

greater on glass than on silicon, respectively. These results suggested that, based on the substrate used, the thickness of the HfO_2 film can be tailored to achieve desired grain structure.

Ellipsometry thicknesses of 58, 127, and 239 nm were determined for the 6.5, 13, and 20-min depositions on silicon, respectively. The models included a SiO_2 interfacial layer and resulted in mean square errors of 0.54, 52, and 7.73 for the 6.5, 13, and 20-min depositions, respectively. The multiple orientations seen by the XRD show that the films were anisotropic, explaining why the ellipsometry data deviated from the Cauchy dispersion model fit. SEM thickness measurements revealed HfO_2 thicknesses ranging from 180 to 230 nm for the 20-min deposition due to crystallite packing on top of a thin layer of SiO_2. The bulk ellipsometry measurements and the SEM measurements were deemed acceptably consistent.

Refractive index and extinction coefficient of the HfO_2 films were also determined from the ellipsometry data. For all three thicknesses, the refractive index was near the expected value of 2 from the literature [28, 33] and the extinction coefficient was near the expected value of zero [61]. These optical measurements confirm that HfO_2 was optically transparent. The FTIR results suggested wavelengths to be avoided, due to interference, if designing a set of fluorescence-based experiments on LOCs.

CV measurements were used to calculate dielectric constant as a function of film area for the 6.5-min deposition. The resulting average dielectric constant was 20.32, which is close to the expected value of 25 [22]. The dielectric constant of HfO_2 is suitable for use as a passivation layer because the layer allows current to pass through into an adjacent fluidic layer while being thick enough to physically isolate the electrodes from the fluidic layer to prevent corrosive degradation.

COMSOL electrostatic simulations were utilized to further explore electric field behaviors through and around the HfO_2 films. Results demonstrated HfO_2 films of 78, 156, and 240 physically passivated the electrodes and enabled the electric field to penetrate into a fluidic layer above the film. Thicker HfO_2 films attenuated the electric potential penetration into the fluid, which was more pronounced at lower frequencies. Conveniently, electrical signal frequency enables straightforward modulation of the potential drop across the dielectric HfO_2 film.

For biological LOC applications, biocompatibility was tested via standard hemolytic potential protocols with human RBCs. When exposed to HfO_2 for up to 5 h, < 1.5% RBC lysis occurred, demonstrating that HfO_2 can be used with minimal reservation in LOC devices interrogating cells.

Implications of this work include increased HfO_2 structural, optical, and electrical film property knowledge as a function of film thickness. These attributes, along with the biocompatibility characteristic are highly useful for LOC applications involving electrokinetic separations and characterizations combined with optical detection of biological samples.

Funding

Funding for S. Habibi provided by the Portage Health Foundation Graduate Assistantship. This work was partially supported by National Science Foundation grants IIP 1414331 and IIP 1632678. H. Moncada-Hernandez was also partially supported by the Michigan Economic Development Corporation (MEDC) Tech Transfer Talent Network (T3N) funding.

Declaration of interest

A.R. Minerick is CTO of MicroDevice Engineering Inc. a startup that utilizes the HfO_2 films in their microchips. P.L. Bergstrom also has interest in MicroDevice Engineering Inc.

References

[1] C.H. Ahn, J.W. Choi, G. Beaucage, J.H. Nevin, J.B. Lee, Disposable Smart lab on a chip for point-of-care clinical diagnostics, Proc. IEEE 92 (2004) 154–173.
[2] R. Martinez-Duarte, Microfabrication technologies in dielectrophoresis applications-A review, Electrophoresis 33 (2012) 3110–3132.
[3] S. Habibi, H. Moncada-Hernandez, H. Lee, A. Minerick, Exploring the Role and Impact of Faradaic Reactions on Hemolysis in Non-Uniform AC Electric Fields (Unpublished Manuscript), (2018).
[4] R. An, K. Massa, D.O. Wipf, A.R. Minerick, Solution pH change in non-uniform alternating current electric fields at frequencies above the electrode charging frequency, Biomicrofluidics 8 (2014).
[5] H. Lee, C. Barber, A. Minerick, Platinum electrode modification: unique surface carbonization approach to improve performance and sensitivity, Electrophoresis 36 (2015) 1666–1673.
[6] S. Ozuna-Chacon, B.H. Lapizco-Encinas, M. Rito-Palomares, S.O. Martinez-Chapa, C. Reyes-Betanzo, Performance characterization of an insulator-based dielectrophoretic microdevice, Electrophoresis 29 (2008) 3115–3122.
[7] A. Gencoglu, A. Minerick, Chemical and morphological changes on platinum microelectrode surfaces in AC and DC fields with biological buffer solutions, Lab Chip 9 (2009) 1866–1873.
[8] Q. Chen, D. Wang, G.Z. Cai, Y.H. Xiong, Y.T. Li, M.H. Wang, H.L. Huo, J.H. Lin, Fast and sensitive detection of foodborne pathogen using electrochemical impedance analysis, urease catalysis and microfluidics, Biosens. Bioelectron. 86 (2016) 770–776.
[9] C. Zhao, M.M. Thuo, X.Y. Liu, A microfluidic paper-based electrochemical biosensor array for multiplexed detection of metabolic biomarkers, Sci. Technol. Adv. Mater. 14 (2013).
[10] A. Wisitsoraat, P. Sritongkham, C. Karuwan, D. Phokharatkul, T. Maturos, A. Tuantranont, Fast cholesterol detection using flow injection microfluidic device with functionalized carbon nanotubes based electrochemical sensor, Biosens. Bioelectron. 26 (2010) 1514–1520.
[11] B. Cetin, D.Q. Li, Dielectrophoresis in microfluidics technology, Electrophoresis 32 (2011) 2410–2427.
[12] S.K. Srivastava, A. Artemiou, A.R. Minerick, Direct current insulator-based dielectrophoretic characterization of erythrocytes: ABO-Rh human blood typing, Electrophoresis 32 (2011) 2530–2540.
[13] H. Lee, C. Barber, A. Minerick, Improving electrokinetic microdevice stability by controlling electrolysis bubbles, Electrophoresis 35 (2014) 1782–1789.
[14] Z. Wang, C. Ivory, A.R. Minerick, Surface isoelectric focusing (sIEF) with carrier ampholyte pH gradient, Electrophoresis (2017), https://doi.org/10.1002/elps.201600565.
[15] L.R. Shang, Y. Cheng, J. Wang, H.B. Ding, F. Rong, Y.J. Zhao, Z.Z. Gu, Double emulsions from a capillary array injection microfluidic device, Lab Chip 14 (2014) 3489–3493.
[16] Y.B. Sawane, S.M. Wadhai, A.V. Limaye, A.G. Banpurkar, Electrolyte concentration effects on DC voltage electrowetting, Sensors Actuators A Phys. 240 (2016) 126–130.
[17] S. Narayanan, M. Nikkhah, J.S. Strobl, M. Agah, Analysis of the passivation layer by testing and modeling a cell impedance micro-sensor, Sensors Actuators A Phys. 159 (2010) 241–247.
[18] O. Buiu, Y. Lu, I.Z. Mitrovic, S. Hall, P. Chalker, R.J. Potter, Spectroellipsometric assessment of HfO2 thin films, Thin Solid Films 515 (2006) 623–626.
[19] A.G. Khairnar, A.M. Mahajan, Effect of post-deposition annealing temperature on RF-sputtered HfO2 thin film for advanced CMOS technology, Solid State Sci. 15 (2013) 24–28.
[20] Y.W. Chen, M.Z. Liu, T. Kaneko, P.C. McIntyre, Atomic layer deposited hafnium oxide gate dielectrics for charge-based biosensors, Electrochem. Solid-State Lett. 13 (2010) G29–G32.
[21] M. Szymanska, S. Gieraltowska, L. Wachnicki, M. Grobelny, K. Makowska, R. Mroczynski, Effect of reactive magnetron sputtering parameters on structural and electrical properties of hafnium oxide thin films, Appl. Surf. Sci. 301 (2014) 28–33.
[22] A.P. Huang, Z.C. Yang, Paul K. Chu, Hafnium-based High-k gate dielectrics, in: P.K. Chu (Ed.), Advances in Solid State Circuit Technologies, InTech, 2010.
[23] Y. Temiz, A. Ferretti, Y. Leblebici, C. Guiducci, A comparative study on fabrication techniques for on-chip microelectrodes, Lab Chip 12 (2012) 4920–4928.
[24] H. Liu, S. Dharmatilleke, D. Maurya, Dielectric materials for electrowetting-on-dielectric actuation, Microsyst. Technol. 16 (2010) 449–460.
[25] J. Lee, H. Moon, J. Fowler, T. Schoellhammer, C.J. Kim, Electrowetting and electrowetting-on-dielectric for microscale liquid handling, Sensors Actuators A Phys. 95 (2002) 259–268.
[26] F. Fassbender, G. Schmitt, M.J. Schoning, H. Luth, G. Buss, J.W. Schultze, Optimization of passivation layers for corrosion protection of silicon-based microelectrode arrays, Sensors Actuators B Chem. 68 (2000) 128–133.
[27] B. Kuswandi, J. Nuriman, W. Huskens, Verboom, Optical sensing systems for microfluidic devices: a review, Anal. Chim. Acta 601 (2007) 141–155.
[28] M. Vargas, N.R. Murphy, C.V. Ramana, Tailoring the index of refraction of nanocrystalline hafnium oxide thin films, Appl. Phys. Lett. 104 (2014).
[29] Z.W. Ma, L.X. Liu, Y.Z. Xie, Y.R. Su, H.T. Zhao, B.Y. Wang, X.Z. Cao, X.B. Qin, J. Li, Y.H. Yang, E.Q. Xie, Spectroscopic ellipsometry and positron annihilation investigation of sputtered HfO2 films, Thin Solid Films 519 (2011) 6349–6353.
[30] C.V. Ramana, M. Vargas, G.A. Lopez, M. Noor-A-Alam, M.J. Hernandez, E.J. Rubio, Effect of oxygen/argon gas ratio on the structure and optical properties of sputter-deposited nanocrystalline HfO2 thin films, Ceram. Int. 41 (2015) 6187–6193.
[31] G. Aygun, I. Yildiz, Interfacial and structural properties of sputtered HfO2 layers, J.

Appl. Phys. 106 (2009).
[32] B. Deng, G. He, J.G. Lv, X.F. Chen, J.W. Zhang, M. Zhang, Z.Q. Sun, Modulation of the structural and optical properties of sputtering-derived HfO2 films by deposition power, Opt. Mater. 37 (2014) 245–250.
[33] D. Franta, I. Ohlidal, D. Necas, F. Vizda, O. Caha, M. Hason, P. Pokorny, Optical characterization of HfO2 thin films, Thin Solid Films 519 (2011) 6085–6091.
[34] Z.W. Ma, Y.Z. Xie, L.X. Liu, Y.R. Su, H.T. Zhao, B.Y. Wang, X.B. Qin, P. Zhang, J. Li, E.Q. Xie, The effect of atomic oxygen treatment on the oxygen deficiencies of Hafnium oxide films, Optoelectron. Adv. Mater. Rapid Commun. 4 (2010) 1493–1496.
[35] G. He, J. Gao, H.S. Chen, J.B. Cui, Z.Q. Sun, X.S. Chen, Modulating the interface quality and electrical properties of HfTiO/InGaAs gate stack by atomic-layer-deposition-derived Al2O3 passivation layer, ACS Appl. Mater. Interfaces 6 (2014) 22013–22025.
[36] B. Dorvel, B. Reddy, J. Go, C. Guevara, E. Salm, C. Duarte Guevara, M. Alam, R. Bashir, Silicon nanowires with high-k hafnium oxide dielectrics for sensitive detection of small nucleic acid oligomers, ACS Nano 6 (2012) 6150–6164.
[37] J. Larkin, R. Henley, D. Bell, T. Cohen Karni, J. Rosenstein, M. Wanunu, Slow DNA transport through nanopores in hafnium oxide membranes, ACS Nano 7 (2013) 10121–10128.
[38] J. Larkin, R. Henley, M. Muthukumar, J. Rosenstein, M. Wanunu, High-bandwidth protein analysis using solid-state nanopores, Biophys. J. 106 (2014) 696–704.
[39] S.H. Shen, I.S. Wang, H. Cheng, C.T. Lin, An enhancement of high-k/oxide stacked dielectric structure for silicon-based multi-nanowire biosensor in cardiac troponin I detection, Sensors Actuators B Chem. 218 (2015) 303–309.
[40] J. Shim, J. Rivera, R. Bashir, Electron beam induced local crystallization of HfO2 nanopores for biosensing applications, Nanoscale 5 (2013) 10887–10893.
[41] J. Oh, H.-J. Jang, W.-J. Cho, M.S. Islam, Highly sensitive electrolyte-insulator-semiconductor pH sensors enabled by silicon nanowires with Al2O3/SiO2 sensing membrane, Sensors Actuators B Chem. 171 (2012) 238–243.
[42] W. Davey, O. Buiu, M. Werner, I.Z. Mitrovic, S. Hall, P. Chalker, Estimate of dielectric density using spectroscopic ellipsometry, Microelectron. Eng. 86 (2009) 1905–1907.
[43] S.K. Srivastava, A. Gencoglu, A.R. Minerick, DC insulator dielectrophoretic applications in microdevice technology: a review, Anal. Bioanal. Chem. 399 (2011) 301–321.
[44] J. Wang, U. Author, R.A. Fava, L.L. Marton, 6.2 Crystallite Size and Lamellar Thickness by X-Ray Methods Crystal Structure and Morphology, (1980).
[45] B.D. Cullity, J.W. Weymout, Elements of X-ray diffraction, Am. J. Phys. 25 (1957) 394–395.
[46] G. He, L.D. Zhang, G.H. Li, M. Liu, L.Q. Zhu, S.S. Pan, Spectroscopic ellipsometry characterization of nitrogen-incorporated HfO2 gate dielectrics grown by radio-frequency reactive sputtering, Appl. Phys. Lett. 86 (2005) 3.
[47] G.M. Xiong, S.J. Yuan, J.K. Wang, A.T. Do, N.S. Tan, K.S. Yeo, C. Choong, Imparting electroactivity to polycaprolactone fibers with heparin-doped polypyrrole: Modulation of hemocompatibility and inflammatory responses, Acta Biomater. 23 (2015) 240–249.
[48] Q. Shi, Q.F. Fan, W. Ye, J.W. Hou, S.C. Wong, X.D. Xu, J.H. Yin, Binary release of ascorbic acid and lecithin from core-shell nanofibers on blood-contacting surface for reducing long-term hemolysis of erythrocyte, Colloids Surf. B: Biointerfaces 125 (2015) 28–33.
[49] M. Ramzan, A.M. Rana, E. Ahmed, M.F. Wasiq, A.S. Bhatti, M. Hafeez, A. Ali, M.Y. Nadeem, Optical characterization of hafnium oxide thin films for heat mirrors, Mater. Sci. Semicond. Process. 32 (2015) 22–30.
[50] D.M. Hausmann, R.G. Gordon, Surface morphology and crystallinity control in the atomic layer deposition (ALD) of hafnium and zirconium oxide thin films, J. Cryst. Growth 249 (2003) 251–261.
[51] D.M. Hausmann, E. Kim, J. Becker, R.G. Gordon, Atomic layer deposition of hafnium and zirconium oxides using metal amide precursors, Chem. Mater. 14 (2002) 4350–4358.
[52] D. Triyoso, R. Liu, D. Roan, M. Ramon, N.V. Edwards, R. Gregory, D. Werho, J. Kulik, G. Tam, E. Irwin, X.D. Wang, L.B. La, C. Hobbs, R. Garcia, J. Baker, B.E. White, P. Tobin, Impact of deposition and annealing temperature on material and electrical characteristics of ALD HfO2, J. Electrochem. Soc. 151 (2004) F220–F227.
[53] H. O'Connor, A. van Riessen, G. Burton, D. Cookson, R. Garrett, Characterisation of standard reference materials using synchrotron radiation diffraction data, Advances in X-ray Analysis, (1999) (This volume).
[54] C.W. Lin, Y.T. Chiang, Tetragonal hafnium oxide film prepared by low-temperature oxidation, Jpn. J. Appl. Phys. 53 (2014).
[55] L. Pereira, P. Barquinha, E. Fortunato, R. Martins, Influence of the oxygen/argon ratio on the properties of sputtered hafnium oxide, Mater. Sci. Eng. B 118 (2005) 210–213.
[56] B.R. Laboratories, Slide Composition Sheet, (2017).
[57] S. Pandey, P. Kothari, S.K. Sharma, S. Verma, K.J. Rangra, Impact of post deposition annealing in O-2 ambient on structural properties of nanocrystalline hafnium oxide thin film, J. Mater. Sci. 27 (2016) 7055–7061.
[58] M. Toledano-Luque, E.S. Andres, A. del Prado, I. Martil, M.L. Lucia, G. Gonzalez-Diaz, F.L. Martinez, W. Bohne, J. Rohrich, E. Strub, High-pressure reactively sputtered HfO2: Composition, morphology, and optical properties, J. Appl. Phys. 102 (2007).
[59] G.E. Jellison, Spectroscopic ellipsometry data analysis: measured versus calculated quantities, Thin Solid Films 313 (1998) 33–39.
[60] Q.H. Phan, Y.L. Lo, Characterization of optical/physical properties of anisotropic thin films with rough surfaces by Stokes-Mueller ellipsometry, Opt. Mater. Express 6 (2016) 1774–1789.
[61] A. Hakeem, M. Ramzan, E. Ahmed, A.M. Rana, N.R. Khalid, N.A. Niaz, A. Shakoor, S. Ali, U. Asghar, M.Y. Nadeem, Effects of vacuum annealing on surface and optical constants of hafnium oxide thin films, Mater. Sci. Semicond. Process. 30 (2015) 98–103.